



# Kesterite monograins for solar cells and water splitting applications

S. Oueslati<sup>a,\*</sup>, M. Pilvet<sup>a</sup>, M. Grossberg<sup>a</sup>, M. Kauk-Kuusik<sup>a</sup>, J. Krustok<sup>a,b</sup>, D. Meissner<sup>a,c</sup>

<sup>a</sup> Department of Materials and Environmental Technology, Tallinn University of Technology, Ehitajate tee 5, 19086 Tallinn, Estonia

<sup>b</sup> Division of Physics, Tallinn University of Technology, Ehitajate tee 5, 19086 Tallinn, Estonia

<sup>c</sup> Crystalsol OÜ, Academia tee 15, 12618 Tallinn, Estonia

## ARTICLE INFO

### Keywords:

Photovoltaics  
Photoelectrochemical  
Storable chemical energy  
Kesterite  
Semiconductor/electrolyte contact  
Water splitting

## ABSTRACT

Photoelectrochemical cells are at the forefront of promising methods of direct solar hydrogen production. It may become the best solution to produce storable chemical energy in a sustainable way and an alternative for combining photovoltaics with expensive storage systems like batteries. This environmentally friendly system based on an earth-abundant kesterite monograins with low processing cost and the outstanding semiconductor properties of single crystals, enables large-scale commercialization. This study aims to evaluate  $\text{Cu}_2\text{ZnSn}(\text{S}_x\text{Se}_{1-x})_4$  monograins with  $x = 0$  to  $x = 1$  for photovoltaic and photoelectrochemical water splitting applications.

## 1. Introduction

Photovoltaics (PV) is the most promising and already today cheapest solution for the future renewable energy supply. However, the use of solar energy-based electricity-producing systems needs completion by a storage system. Photoelectrochemical (PEC) cells, which convert solar energy directly into chemical energy, are promising solutions to the storage problem in PV. Direct production of clean and storable chemical fuels such as hydrogen from solar energy is of utmost importance for future sustainable post-carbon energy systems [1]. It is therefore vital to develop efficient processes to convert the sunlight into chemical energy to meet the commercial-scale demand. The theoretical background of photoelectrochemistry, i.e. the development of theories describing the processes occurring at the semiconductor/electrolyte interface, was developed already in the 1960s, mainly by Heinz Gerischer and Rüdiger Memming [2]. Nevertheless, until now, various problems and challenges have been encountered in terms of the material selection, stability, and efficiency of PEC cells. Ordinarily, materials with a high bandgap ( $E_g$ ) would be preferred to account for overpotentials and other losses within the device [3]. But these materials either have poor chemical stability under working conditions or suffer from limited light absorption, as is the case for  $\text{TiO}_2$  [4]. Platinum (Pt) or similar metals are often added to the surface to prevent degradation and act as co-catalysts to lower the overpotentials for hydrogen evolution reaction (HER). But this in turn has pronounced economic and environmental costs. The development of efficient, stable, and low-cost material is an essential prerequisite for

achieving the desired electrochemical hydrogen production from water splitting. Thereupon, kesterites as earth-abundant materials with low processing cost and outstanding light absorption properties, are interesting candidates for PV and photoelectrochemical application in particular in the form of monograin membranes. The latter membranes consist of separately grown mono-crystalline absorber crystals embedded into an organic resin foil so that every grain sticks out on both sides. For PV application, the solar cells are finished by adding a CdS buffer layer followed by sputtering of a bilayer  $i\text{-ZnO}/\text{ZnO}:\text{Al}$  as a front contact and graphite paste as a back contact. The latter structure leads to versatile flexible, and lightweight solar cells, which exhibit numerous advantages compared to the major technologies used nowadays for manufacturing solar cells, i.e. the planar and the thin-film technologies. The greatest benefit of monograin technology lies in the simplicity of making unlimited areas and shapes of single-crystalline absorbers. In addition to the advantage of growing the material at a relatively high temperature, the chemical in-composition and the size of the powder grains can be easily controlled leading to a uniform distribution of chemical composition and doping concentration after the synthesis. Moreover, the separation of thermal and chemical processes for absorber production from the device production, has made the monograin technology one of the cheapest technologies for continuous, high throughput roll-to-roll technology. In addition, long accelerated heat tests of monograin-based kesterite cells did not show any significant degradation, which makes this technology quite advanced, and in particular ready for flexible PV applications [5]. The disadvantage of the

\* Corresponding author.

E-mail address: [souhaib.oueslati@taltech.ee](mailto:souhaib.oueslati@taltech.ee) (S. Oueslati).

<https://doi.org/10.1016/j.tsf.2021.138981>

Received 18 June 2021; Received in revised form 22 October 2021; Accepted 27 October 2021

Available online 31 October 2021

0040-6090/© 2021 Elsevier B.V. All rights reserved.

monograin based kesterite technology is the limited devices efficiency which is a general challenge for the kesterite community.

The kesterite based monograin membranes can also be used as photocathodes. In recent years,  $\text{Cu}_2\text{ZnSnS}_4$  (CZTS) became widely used as a photocathode for the production of hydrogen from solar water splitting. Yokoyama et al. first demonstrated in 2010 the application of CZTS as a photocathode [6]. The CZTS photocathode performance and stability were enhanced through a series of surface modifications by adding CdS and  $\text{TiO}_2$  layers to accelerate charge transfer and to protect the lower layer from corrosion in acid/alkaline solution, respectively [6]. Another type of band structure that was studied uses a CZTS/CdS/ $\text{TiO}_2$ /Pt photocathode, so the photogenerated electrons easily migrated from the CZTS to the CdS, and then, through  $\text{TiO}_2$ , into the Pt catalyst to generate  $\text{H}_2$  gas [6]. Using this structure, the highest  $\text{H}_2$  production to solar energy efficiency of about 1.2% was presented, corresponding to a photocurrent density of about  $9 \text{ mA/cm}^2$  [7]. By improving the quality of the CZTS layer, Yang et al. reported a photocurrent using a similar structure of about  $13 \text{ mA/cm}^2$  [8].

Further improvement of  $\text{H}_2$  generation efficiency of about 7% was achieved by optimizing the thickness of the additional  $\text{TiO}_2$  protecting layer on CZTS, deposited by atomic layer deposition [9]. More recent work demonstrated an efficiency of about 3.5% for a CdS/CZTS based thin film photocathode using surface plasmon resonance effect of a Pt-nano-particles-modified  $\text{TiO}_2$  nanoball [10].

Due to the toxicity of Cd and the instability problem of CdS, an  $\text{In}_2\text{S}_3$ /CdS double layer on top of the CZTS film was proposed in conjunction with a Pt catalyst [11]. The photocathode showed a significant improvement of stability and achieved a half-cell solar-to-hydrogen efficiency of 1.63% [11]. The authors further demonstrated a bias-free PEC water splitting system by combining the above CZTS cathodes with a  $\text{BiVO}_4$  counter photoanode. Another protective layer was suggested by Dingwang et al. based on  $\text{HfO}_2$  photocorrosion-resistant film deposited by atomic layer deposition to protect the CdS-covered CZTS photocathode surface. The authors reported over 1% efficient unbiased stable solar water splitting based on a sprayed CZTS photocathode and reported a significant stability improvement after adding  $\text{HfO}_2$  [12].

Another strategy to upgrade the PEC performance of kesterite photocathodes is by adjusting the  $E_g$  and the position of conduction ( $E_{CB}$ ) and valence ( $E_{VB}$ ) bands without adding additional layers that could be unstable like CdS or precious like Pt. The band position could be adjusted by appropriate cation or/and anion substitution [13,14] and could be an efficient and low-cost way to improve the PEC performance of the kesterite photocathode. Ying et al. reported an improvement of CZTS photocathode bulk properties using the partial Cd substitution method [15]. A  $\text{Cu}_2\text{Cd}_{0.4}\text{Zn}_{0.6}\text{SnS}_4$  photoabsorber coated with CdS/ $\text{TiMo}$ /Pt is reported to yield a photocurrent of  $17 \text{ mA cm}^{-2}$  comparing to  $4 \text{ mA cm}^{-2}$  at 0V versus reversible hydrogen electrode using pristine CZTS coated with CdS/ $\text{TiMo}$ /Pt [15].

In this work, we study the anion substitution effect in the kesterite material  $\text{Cu}_2\text{ZnSn}(\text{S}_x\text{Se}_{1-x})_4$  (CZTSSe) on the PEC and the PV performance. The work is based on a promising approach consisting of implementing kesterite material as monograin membranes, in which semiconductor particles are embedded into a polymer film so that they stick out from one side and act as an active layer (Fig. 1a). The band positions of CZTSSe with different sulphur content are important parameters for PV and PEC cells. We sought to extract the flat-band position  $E_{FB}$ ,  $E_{CB}$  and  $E_{VB}$  for our kesterite materials with different Sulphur content using the Mott-Schottky method. We offer complete sets of experimental data obtained with each fabricated material, and we finish by plotting the extracted parameters in one energy diagram scheme.

## 2. Experimental

The investigated absorber layers consist of single-crystalline powder so-called "Monograins" synthesized using elemental precursors Cu, Zn, Sn, Se, and S, in form of powder with a purity of 99.999% purchased

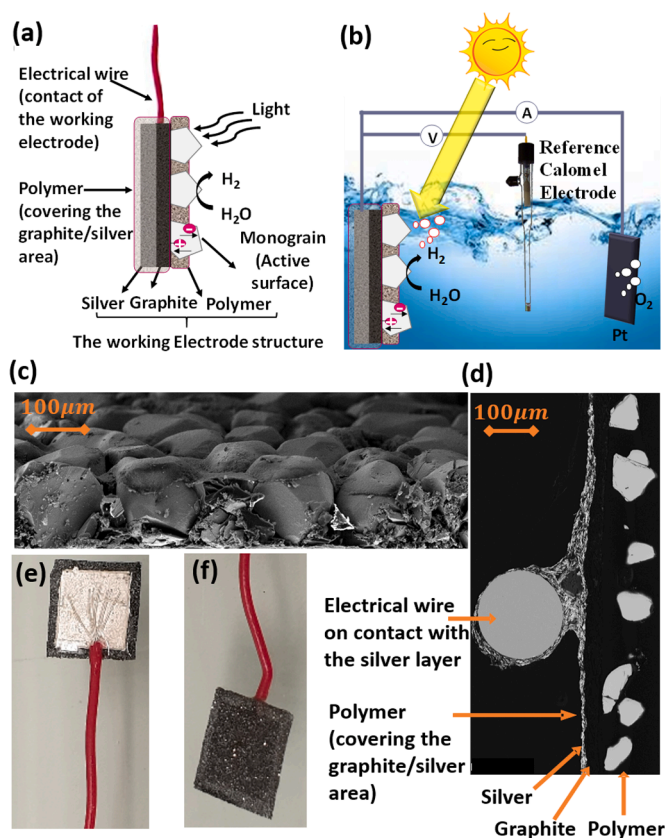


Fig. 1.. Scheme (a) and SEM picture (d) of Monograin layer (MGL) finished as photocathode for water splitting application, (b) Scheme of a three-electrode cell configuration using MGL photocathode. (c) SEM picture of a MGL. Photo of the working electrode (e) back-side (f) front-side.

from Alfa Aesar. The precursors were mixed with potassium iodide (KI) and inserted into quartz ampoules. Then, the ampoules were degassed and sealed under vacuum conditions. The kesterite monograins can be obtained at temperatures above the melting point of the used salt KI ( $681^\circ\text{C}$ ) and at temperatures lower than the melting point of the semiconductor (CZTSSe) itself ( $\sim 940^\circ\text{C}$ ). The sealed ampoules were heated up to  $740^\circ\text{C}$  with a heating rate of about  $4^\circ\text{C}/\text{min}$  and the kesterite monograins were synthesized at the optimized temperature  $740^\circ\text{C}$  in molten KI flux material for 88 h. Then, the ampoules were taken out of the oven and naturally cooled to room temperature. The final product consists of single crystals kesterite material grown in different sizes and stick to each other by the solidified flux KI. The KI was removed by washing the materials with deionized water at room temperature. After that the monograins were dried and sieved to the narrow fractions of about 100 to 120  $\mu\text{m}$ . An isothermal heat treatment step at  $740^\circ\text{C}$  for 35 min is needed to heal the monograin's surface after washing and sieving steps.

The  $[\text{S}]/([\text{S}]+[\text{Se}])$  ratio is varied in this study and presented as  $x$  throughout the manuscript, referring to the input compositional ratio introduced to the system. The compositional ratios used in the synthesis mixture investigated here are  $x = 0, 0.2, 0.4, 0.6, 0.8$  and 1 given in the figures and in the text as initial  $x$ , where the samples  $x = 0$  and  $x = 1$  represent the pure phases CZTSSe and CZTS, respectively.

The fabrication of the photocathode and solar cell devices started with the formation of a photoactive membrane so-called monograin layers (MGL). An organic resin (epoxy) layer stripe with a controlled thickness was applied by the doctor blade method on a temperature stable plastic foil. The applied thickness is approximately 40% of the size of the sieved monograins. A monolayer of the synthesized grains was immersed into the epoxy layer to form the MGL. The upper part of the

grains (approximately 60% of the grain size) remained uncovered by the epoxy as shown in Fig. 1c, and it is photoactive.

The fabricated MGL membranes from each investigated material were cut in two parts. The first half membrane was finished as a classical solid state solar cell by adding a CdS buffer layer by chemical bath deposition to form the *p-n* heterojunction followed by sputtering of a bilayer *i-ZnO/ZnO:Al* as a front contact. Once the front contact is established, the plastic foil substrate was removed. Then, by mechanical abrasion, the epoxy covering the grains from the backside was polished away. The opened grains surface was covered by graphite paste to form the back contact. A more detailed description of monograin synthesis and solar cell preparation can be found elsewhere [13,14].

The second half membrane was finished as a photocathode. As in the case of making the solid state solar cell, the epoxy covering the grains from the backside of the MGL is removed by mechanical abrasion. After this polishing, a graphite and silver paste are applied through a mask with a 1 cm<sup>2</sup> area and an electric wire is attached to it to form the back contact. Finally, the whole backside area is encapsulated with epoxy ensuring that the only charge conductivity from the backside is through the attached electrical wire. The working electrode structure is illustrated in the scheme presented in Fig. 1a and the scanning electron microscope (SEM) picture presented in Fig. 1d. Photos of the back and the front side of the working electrode are provided in Fig. 1e and Fig. 1f respectively.

The composition of the monograins was characterized using Energy Dispersive X-ray Spectroscopy (EDX) using Zeiss MERLIN scanning electron microscope operated with an accelerating voltage of 20 kV using a Röntec EDX XFlash 3001 detector.

The current-voltage (J-V) measurements at room temperature were performed under AM1.5 illumination conditions using a Newport Oriel solar simulator system. The external quantum efficiency (EQE) was measured in short circuit condition using a calibrated halogen lamp and an SPM-2 prism monochromator. Monochromatic chopped light is focused on the active surface of the fabricated solar cell and the resulting current was detected using a DSP Lock-In amplifier (SR 810).

The PEC properties of the fabricated CZTSSe photocathodes were investigated in a three-electrode cell using the photocathodes as working electrodes (WE), a Pt counter electrode (CE) and a saturated calomel electrode as reference electrode, respectively. H<sub>2</sub>SO<sub>4</sub> aqueous solution (0.1M, pH = 1.4) was used as an electrolyte. The schematic diagram of the three-electrode cell is indicated in Fig. 1b. The potential-current characteristics were carried out by means of an electrochemical analyzer (PGZ100 Voltalab). All the photocurrent curves were measured under 100 mW/cm<sup>2</sup> illumination using calibrated intensity from a halogen lamp and given with respect to the normal hydrogen electrode (NHE) reference scale. The measurement was performed under three conditions, namely: dark, steady illumination, and chopped light.

The same three-electrode configuration described above was used to measure the electrochemical impedance of the investigated photocathodes. H<sub>2</sub>SO<sub>4</sub> aqueous solution (0.1M, pH = 1.4) was used as an electrolyte. The potentiostat used in this case is the modular electrochemical instrument Autolab PGSTAT30. The measurements were carried out in the dark and the impedance-frequency data were recorded from 0.1 Hz to 10<sup>5</sup> Hz at 0 V/V<sub>NHE</sub>, whereas the impedance-voltage measurement was carried out at 30 kHz.

### 3. Results and discussion

EDX analysis confirmed that the ratio of [S]/([S]+[Se]) in synthesized was similar to input values. The synthesized CZTSSe monograins were slightly Cu-poor and Zn-rich as presented in table 1. A comprehensive photoluminescence and Raman study of CZTSSe monograins with different x amounts can be found elsewhere [16].

The first half of the prepared membranes were finished as solar cells. A current-voltage characterization of the solar cells was carried out, and the values of the open-circuit voltage  $V_{OC}$ , short-circuit current  $J_{SC}$ , fill factor  $FF$ , conversion efficiency  $\eta$ ,  $E_g$ ,  $V_{OC}$  deficit of the solar cells, are summarized in Table 2. From each material with different x amounts, four cells are fabricated. In total, 24 solar cells were included in this study. Standard variations of J-V parameters were calculated and presented in table 2, and they show a minor variation between the parameters of the solar cells. The J-V curve of the best solar cells for each material is presented in Fig. 2a. The area of the solar cells is about 3.8 mm<sup>2</sup>, and the presented  $\eta_{active}$  values are adjusted to the active area of the material. The  $\eta_{active}$  of solar cells show a maximum for the CZTSSe material with x = 0.4 and 0.6, although those devices don't exhibit the lowest  $V_{OC}$  deficit. For the high Se content material (x < 0.6), the solar cells show a tendency for lower performance due to the lower  $FF$  values. The decrease in  $FF$  with increasing Se content suggests that the band alignment is inappropriate for the kesterites with high Se content and the CdS buffer layer, whereas the voltage-loss seems to be the main limiting factor for kesterite material with the high S content.  $V_{OC}$  and  $J_{SC}$  showed the tendency expected for the change in x.

The EQE was measured under chopped light in the wavelength range between 350 nm and 1450 nm. The normalized EQE spectra of the investigated cells are presented in Fig. 2b. All the devices show losses in the short wavelength region due to the absorption in the CdS buffer layer. The maximum carrier collection is seen at a wavelength of around 540 nm for the samples with x = 1, 0.8, and 0.6, and declining in the longer wavelength region defining the material  $E_g$ . The cells fabricated from materials with high Se content show maximum carrier collection at a longer wavelength region suggesting better charge collection for photons absorbed deeper in the material. For more precise estimation of the  $E_g$ , ( $EQE \cdot E$ )<sup>2</sup> was plotted versus the photon energy. The  $E_g$  is extracted from the interception of the linear part with the energy axis [14]. Depending on the x, the  $E_g$  of the kesterite monograins is found to be tuned between 0.98 and 1.55 eV. The  $V_{OC}$  deficit are calculated using the extracted  $E_g$  from the EQE data and presented in Table 2.

The second half of the prepared membranes were finished as photocathodes. The current- potential measurement of the photocathode using monograins with different x is presented in Fig. 3. The negative current observed in the dark (black line) was not expected to occur as the current should theoretically be zero. Possible reasons could be: (i) possible electrochemical reaction at the metal backside contact, although it is unlikely since we made sure it was properly sealed during the course of fabrication, (ii) electrochemical reaction occurring at the surface of the WE caused by elemental metals or secondary phases (ZnS, Cu<sub>x</sub>S, SnS<sub>x</sub>) on the kesterite surface; (iii) direct diffusion (or tunneling) of electrons from the valence band to protons at the hydrogen formation potential. In the latter case water is reduced in the dark due to a non-ideal valence band position (slightly positive of the hydrogen

**Table 1.**  
The chemical composition and the corresponded ratios after synthesis as measured by EDX.

x	Cu	Zn	Sn	S	Se	Cu/Zn+Sn	Zn/Sn	(S+Se)/M	S/(S+Se)
x = 1	1.89	1.11	1.00	4.01	0.00	0.90	1.11	1.00	1.00
x = 0.8	1.91	1.02	1.00	3.16	0.76	0.95	1.02	1.00	0.81
x = 0.6	1.95	1.05	1.00	2.46	1.51	0.95	1.05	0.99	0.62
x = 0.4	1.88	1.03	1.00	1.63	2.33	0.92	1.03	1.01	0.41
x = 0.2	1.88	1.00	1.00	0.82	3.11	0.94	1.00	1.01	0.21
x = 0	1.74	0.99	1.00	0.00	3.75	0.87	0.99	1.01	0.00

**Table 2.**  
Summary of the photovoltaic and the electrochemical behaviors of  $\text{Cu}_2\text{ZnSn}(\text{S}_x\text{Se}_{1-x})_4$  cells.

x	Photovoltaic Behavior						Electrochemical Behavior				$N_A/\text{cm}^3$
	$R_s$ , $\pm 0.5 [\Omega \cdot \text{cm}^2]$	$R_{sh}$ , $\pm 25 [\Omega \cdot \text{cm}^2]$	$V_{OC}$ , $\pm 15 [\text{mV}]$	FF, $\pm 1 [\%]$	$J_{SC}$ , $\pm 0.5 [\text{mA}/\text{cm}^2]$	$\eta_{active}$ , $\pm 0.2 [\%]$	$E_g$ $\pm 0.02 [\text{eV}]$	$V_{OC}$ deficit, [mV]	$E_{FB}$ , $\pm 0.01 [E_{NHE}]$	$E_{VB}$ , $\pm 0.01 [E_{NHE}]$	
1	1.7	1124	723	65.2	18.1	8.5	1.55	827	0.25	0.43	$9.2 \times 10^{15}$
0.8	2.1	675	665	59.1	20.3	8.0	1.46	795	0.08	0.29	$2.9 \times 10^{15}$
0.6	1.3	551	597	62.9	23.2	8.7	1.39	793	0.06	0.20	$4 \times 10^{16}$
0.4	1.6	344	513	58.0	30.0	8.9	1.26	747	-0.03	0.16	$6.3 \times 10^{15}$
0.2	1.1	224	441	52.4	32.4	7.4	1.11	669	-0.08	0.10	$7.4 \times 10^{15}$
0	1.6	158	364	51.9	33	6.23	0.98	616	-0.01	0.14	$2.7 \times 10^{16}$

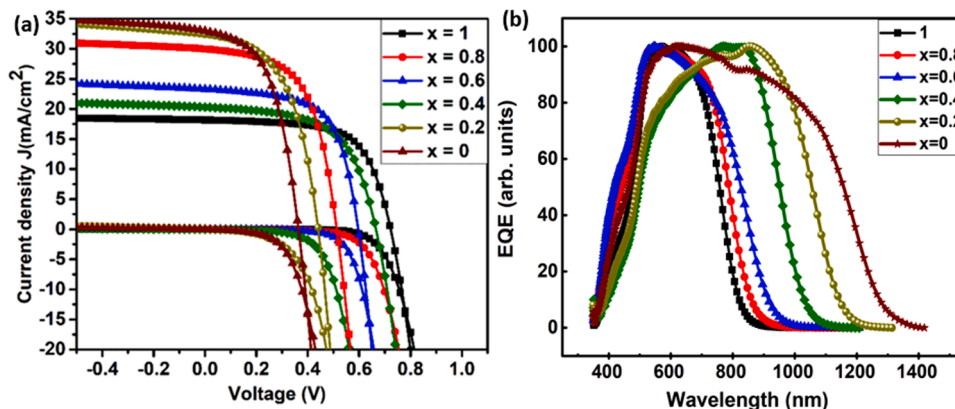


**Fig. 2.** J-V curves measured under AM1.5 illumination (a) EQE curves (b) of  $\text{Cu}_2\text{ZnSn}(\text{S}_x\text{Se}_{1-x})_4$  based monograin solar cells as a function of input x concentration.

formation potential). This was confirmed by the flatband potential measurements given below. The highest dark current is seen in the case  $x = 0$  whereas the lowest appears for  $x = 1$ . Under illumination (red line), a more pronounced negative photocurrent at negative potentials reveals the ability of the investigated materials to conduct photoelectrochemical water reduction reaction. An exponential decrease of the light current was observed at potentials negative of the hydrogen formation potential (0 V/ $V_{NHE}$ ). The latter is a characteristic of a photoelectrochemical reaction that occurs on the interface electrode/electrolyte related to HER. Since the exponential increase of current density occurs only at negative potentials, the cells do not provide a photovoltage to operate as photoanodes. This means a large overpotential is needed for hydrogen evolution using kesterites.

For better photocurrent evaluation, the chopped light condition is presented (blue line) for all the x cases. A higher current step reveals a higher generated photocurrent (light current minus dark current). In the case of  $x = 0$ , the saturated dark current is the lowest, which corresponds to the lowest charge transfer-ability at the electrode/electrolyte interface. These high overpotentials indicate the importance of adding a catalyst to the electrodes surfaces.

At the semiconductor-electrolyte interface, space charge regions are formed in the semiconductor as well as the electrolyte due to the equilibration of the chemical potentials of semiconductor and electrolyte (here called redox potential) [17]. The junction can be modeled as a double capacitor. The first capacitor models, the space charge region (depletion layer) in the semiconductor side at equilibrium, and the second models, the electrical double layer of opposite sign in the electrolyte (Helmholtz layer). Therefore, the total capacitance of the interfacial double layer,  $C_{interface}$ , includes contributions from semiconductor capacitance ( $C_{SC}$ ) and the capacitance of the Helmholtz layer in the electrolyte ( $C_H$ ) in series with each other  $1/C_{interface} = 1/(C_{SC} + 1/C_H)$  [18]. For most cases, the semiconductor-electrolyte interface has a finite resistance value, and the equivalent circuit commonly used for modeling consists of the two capacitances in series with a (series) resistor, in

parallel to a (parallel) resistor [18]. The semiconductor capacitance will vary with the extent of band bending, i.e. with the applied voltage, while the  $C_H$  is expected to remain constant. Hence, it is often assumed that  $C_H \gg C_{SC}$  such that  $C_{SC}$  is approximately  $C_{interface}$  [18]. Through this manuscript, the experimentally calculated capacitance is considered as  $C_{SC}$ , and the insert in Fig. 4b represents the used equivalent circuit.

During an electrochemical impedance spectroscopy experiment, the impedance in the dark is recorded while applying an alternating current signal for various frequencies,  $f$  ( $0.1 \text{ Hz} < f < 10^5 \text{ Hz}$ ), superimposed on a bias voltage. In Fig. 4a, the capacitance steps function of frequency is presented and shows a monotonic decrease until it reaches a plateau at frequencies higher than 1 kHz. Therefore, the chosen frequency for the evaluation of the impedance versus voltage is  $f = 30 \text{ kHz}$ , assuming that there is no contribution of deep defects at the chosen frequency.

The  $E_{FB}$ , one of the important characteristic parameters of the semiconductor-electrolyte junction, has been estimated using various techniques [18]. The most popularly used technique is the Mott-Schottky method based on the following equation for p-type material [19]:

$$\frac{1}{C_{SC}^2} = \frac{-2}{\epsilon \epsilon_0 q N_A} \left( E - E_{FB} - \frac{kT}{q} \right) \quad (1)$$

Where  $\epsilon$  is the relative permittivity,  $\epsilon_0$  is the electrical permittivity of free space,  $q$  is the elementary charge,  $N_A$  is the acceptor doping levels,  $E_{FB}$  is the flatband potential,  $E$  is applied potential,  $k$  is the Boltzmann constant and  $T$  is the temperature.

For determining the flat band potential, the impedance is measured as function of the applied potential at 30 kHz for all the investigated electrodes.  $1/C_{interface}^2$  is plotted as a function of the applied potential, as shown in Fig. 4b for the electrode with  $x = 1$ . The Mott-Schottky plots show a linear behavior for a range of applied potential, and the  $E_{FB}$  is determined from the interception with the potential axis [18]. Another important parameter extracted from the Mott-Schottky plot is the  $N_A$ , which is inversely proportional to the slope of the linear part. The latter

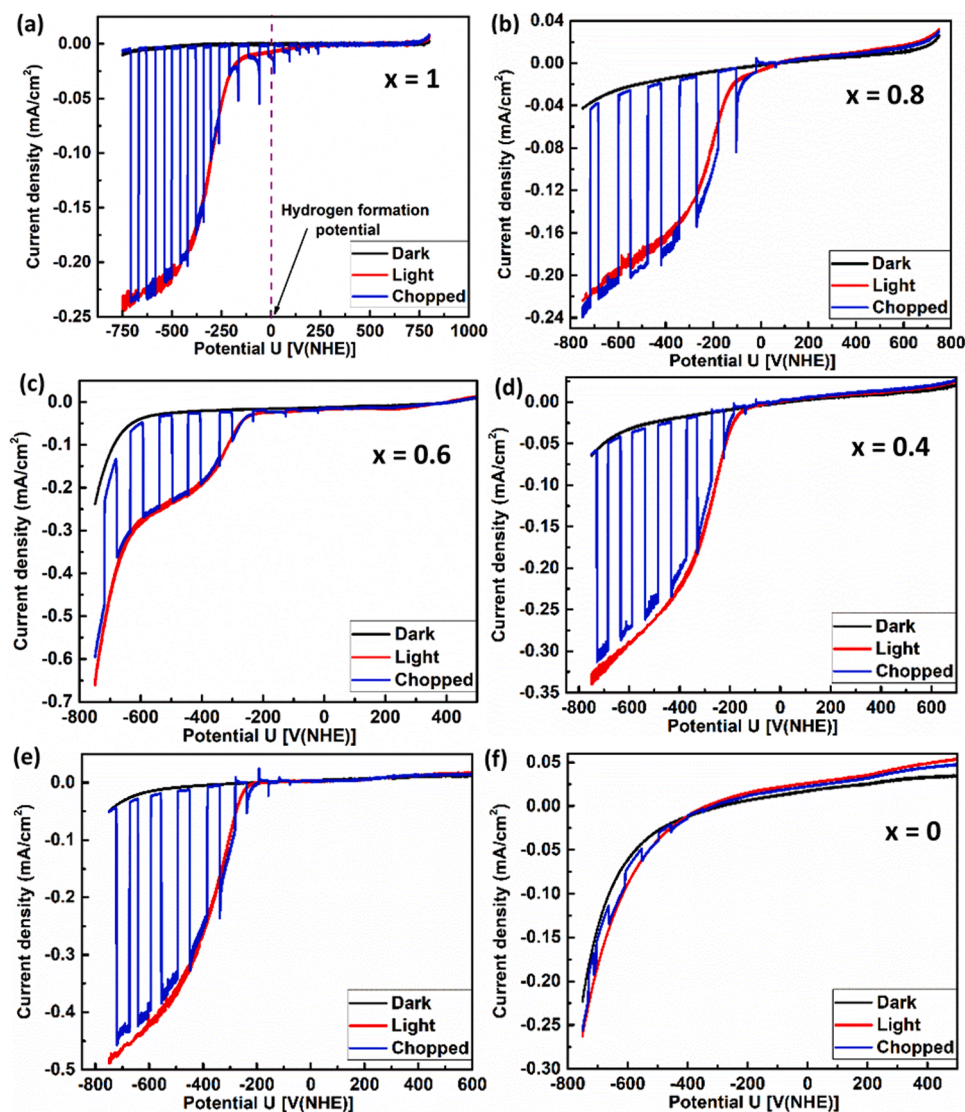


Fig. 3.. Current-potential (J-V) characteristics of  $\text{Cu}_2\text{ZnSn}(\text{S}_x\text{Se}_{1-x})_4$  PEC were measured for every working electrode with different x values.

parameters are vital to calculate the valence band edge positions on the NHE reference scale. For a *p*-type semiconductor,  $E_{VB}$  is calculated as [17]:

$$E_{VB} = E_{FB} + \frac{kT}{q} \ln \left( \frac{N_V}{N_A} \right) \quad (2)$$

where  $E_{VB}$  is the valence band position,  $E_{FB}$  is flat band potential,  $k$  is Boltzmann constant,  $N_V$  is the effective density of states at the valence band edge (typically  $\sim 10^{19} \text{ cm}^{-3}$  [12]) and  $N_A$  is the acceptor concentration obtained from Mott-Schottky plot.

The negative slope in Fig. 4b confirms the *p*-type conductivity of the investigated materials, which is in good agreement with the cathodic photocurrent.  $E_{VB}$  and doping levels were calculated using equations (1) and (2), respectively. The results are summarized in Table 1.

The change of the slope when reaching the redox potential of the solution and starting to reduce protons indicates the shift of flat band potential with changing the pH at the kesterite interface to the solution. Considering the extracted parameters above, it is imperative to present the  $E_{CB}$  and  $E_{VB}$  on the energy scale for all the investigated materials, as presented in Fig. 5.

Considering that the band edge position of the conduction and valence band should straddle the water redox potential, a reasonable

amount of overpotential is needed to pilot the hydrogen and oxygen formation reaction. Fig. 5 shows the values for our kesterite electrodes of different ratio of  $[\text{S}]/([\text{S}]+[\text{Se}])$ , a case where the conduction bands are much more negative than the hydrogen formation potential. Even the valence band are getting close or even above the hydrogen potential (far negative of the oxygen formation potential). For  $x = 0$  to 0.4 the valence band even is negative of the hydrogen potential, which explains the hydrogen formation in the dark. Nevertheless, starting only at around  $-600 \text{ mV}$  indicates the high overpotentials needed at the non-modified kesterite interface.

#### 4. Conclusion

Kesterite monograins with different ratios of  $[\text{S}]/([\text{S}]+[\text{Se}])$ , were fabricated and evaluated for PV and PEC water splitting applications. The highest solar efficiencies are measured using CZTSSe materials ( $x = 0.6, 0.4$ ) and decrease when using the pure phases CZTS and CZTSe. All the investigated electrodes possess valence band positions close to the hydrogen potential formation, which even leads to the injection of electrons from the valence band to the electrolyte for the electrodes with higher selenium content, which leads to a shift of the flat band potential for negative potentials. Very high overpotentials indicate a need for a catalyst to the active surface of the kesterite electrodes. Modifying the

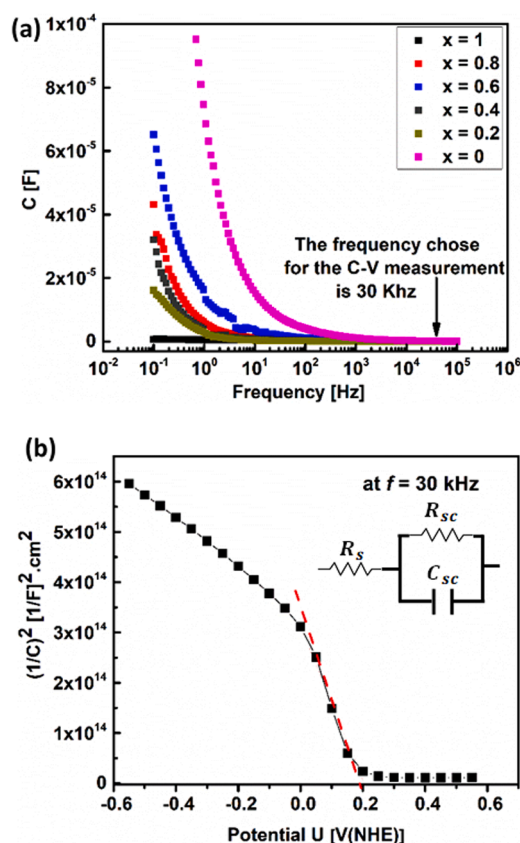


Fig. 4.. (a) Capacitance values versus frequency for electrodes with different  $x$  contents. (b) example of a Mott-Schottky plot of the  $x = 1$  case at 30 kHz.

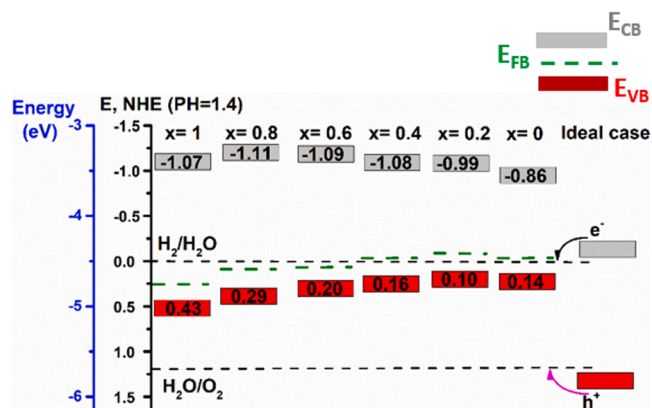


Fig. 5.. Positions of energy band edges for all  $x$  with respect to the normal hydrogen electrode (NHE) potential and vacuum energy (eV) and the ideal band position for water splitting reaction.

surface of the kesterite by introducing a hole barrier for the valence band such as  $\text{SnO}_2$ , and adding a catalyst for the electron transfer, is vital for the investigated electrodes. Without modification all kesterite photocathodes investigated do not provide a photovoltage for CE added for a water splitting device due to their too negative band position.

#### Declaration of Competing Interest

The authors declare the following financial interests/personal relationships which may be considered as potential competing interests:

Maarja Grossberg reports financial support was provided by European Regional Development Fund. Souhaib Oueslati reports financial

support was provided by Estonian Research Council grant.

#### Acknowledgement

The study was financially supported by the Estonian Research Council grant PRG1023 and PSG441, by the European Regional Development Fund project TK141, and TalTech grant SSGF21005.

#### References

- [1] T.R. Cook, D.K. Dogutan, S.Y. Reece, Y. Surendranath, T.S. Teets, D.G. Nocera, Solar energy supply and storage for the legacy and nonlegacy worlds, *Chem. Rev.* 110 (2010) 6474–6502, <https://doi.org/10.1021/cr100246c>, <https://doi.org/>.
- [2] R. Memming, Charge Transfer Processes at the Semiconductor-Liquid Interface, Chap 7. Semiconductor Electrochemistry, Wiley-VCH, 2000, p. 515, 240, <http://doi.wiley.com/10.1002/9783527613069>.
- [3] R. Van De Krol, Y. Liang, J. Schoonman, Solar hydrogen production with nanostructured metal oxides, *J. Mater. Chem.* 18 (2008) 2311–2320, <https://doi.org/10.1039/b718969a>, <https://doi.org/>.
- [4] W. Yang, R.R. Prabhakar, J. Tan, S.D. Tilley, J. Moon, Strategies for enhancing the photocurrent, photovoltage, and stability of photoelectrodes for photoelectrochemical water splitting, *Chem. Soc. Rev.* 48 (2019) 4979–5015, <https://doi.org/10.1039/c8cs00997j>, <https://doi.org/>.
- [5] G. Larramona, C. Choné, D. Meissner, K. Ernits, P. Bras, Y. Ren, R. Martín-Salinas, J.L. Rodríguez-Villatoro, B. Vermang, G. Brammert, Stability, reliability, upscaling and possible technological applications of kesterite solar cells, *JPhys Energy* 2 (2020), <https://doi.org/10.1088/2515-7655/ab7cee> <https://doi.org/>.
- [6] D. Yokoyama, T. Minegishi, K. Jimbo, T. Hisatomi, G. Ma, M. Katayama, J. Kubota, H. Katagiri, K. Domen, H $_2$  evolution from water on modified Cu $_2$ ZnSnS $_4$  photoelectrode under solar light, *Appl. Phys. Express.* 3 (2010), <https://doi.org/10.1143/APEX.3.101202> <https://doi.org/>.
- [7] A.S. Nazligul, M. Wang, K.L. Choy, Recent development in earth-abundant kesterite materials and their applications, *Sustain* 12 (2020), <https://doi.org/10.3390/su12125138> <https://doi.org/>.
- [8] W. Yang, Y. Oh, J. Kim, M.J. Jeong, J.H. Park, J. Moon, Molecular Chemistry-Controlled Hybrid Ink-Derived Efficient Cu $_2$ ZnSnS $_4$  Photocathodes for Photoelectrochemical Water Splitting, *ACS Energy Lett* 1 (2016) 1127–1136, <https://doi.org/10.1021/acsenenergylett.6b00453>, <https://doi.org/>.
- [9] C. Ros, T. Andreu, S. Giraldo, V. Izquierdo-Roca, E. Saucedo, J.R. Morante, Turning Earth Abundant Kesterite-Based Solar Cells into Efficient Protected Water-Splitting Photocathodes, *ACS Appl. Mater. Interfaces.* 10 (2018) 13425–13433, <https://doi.org/10.1021/acsami.8b00062>, <https://doi.org/>.
- [10] L. Li, K. Feng, D. Huang, K. Wang, Y. Li, Z. Guo, Y.H. Ng, F. Jiang, Surface plasmon resonance effect of a Pt-nano-particles-modified TiO $_2$  nanoball overlayer enables a significant enhancement in efficiency to 3.5% for a Cu $_2$ ZnSnS $_4$ -based thin film photocathode used for solar water splitting, *Chem. Eng. J.* 396 (2020), <https://doi.org/10.1016/j.cej.2020.125264> <https://doi.org/>.
- [11] F. Jiang, T. Harada Gunawan, Y. Kuang, T. Minegishi, K. Domen, S. Ikeda, Pt/In $_2$ S $_3$ /CdS/Cu $_2$ ZnSnS $_4$  Thin Film as an Efficient and Stable Photocathode for Water Reduction under Sunlight Radiation, *J. Am. Chem. Soc.* 137 (2015) 13691–13697, <https://doi.org/10.1021/jacs.5b09015>, <https://doi.org/>.
- [12] D. Huang, K. Wang, L. Yu, T.H. Nguyen, S. Ikeda, F. Jiang, Over 1% Efficient Unbiased Stable Solar Water Splitting Based on a Sprayed Cu $_2$ ZnSnS $_4$  Photocathode Protected by a HfO $_2$  Photocorrosion-Resistant Film, *ACS Energy Lett* 3 (2018) 1875–1881, <https://doi.org/10.1021/acsenenergylett.8b01005>, <https://doi.org/>.
- [13] S. Oueslati, M. Grossberg, M. Kauk-Kuusik, V. Mikli, K. Ernits, D. Meissner, J. Krustok, Effect of germanium incorporation on the properties of kesterite Cu<math>\_{2-x}</math>ZnSn(S,Se)<math>\_{4-x}</math> monograins, *Thin Solid Films* 669 (2019), <https://doi.org/10.1016/j.tsf.2018.11.020> <https://doi.org/>.
- [14] S. Oueslati, M. Kauk-Kuusik, C. Neubauer, V. Mikli, D. Meissner, G. Brammert, B. Vermang, J. Krustok, M. Grossberg, Study of (Ag $_x$ Cu $_{1-x}$ ) $_2$ ZnSn(S,Se) $_4$  monograins synthesized by molten salt method for solar cell applications, *Sol. Energy.* 198 (2020) 586–595, <https://doi.org/10.1016/j.solener.2020.02.002>, <https://doi.org/>.
- [15] Y.F. Tay, H. Kaneko, S.Y. Chiam, S. Lie, Q. Zheng, B. Wu, S.S. Hadke, Z. Su, P. S. Bassi, D. Bishop, T.C. Sum, T. Minegishi, J. Barber, K. Domen, L.H. Wong, Solution-Processed Cd-Substituted CZTS Photocathode for Efficient Solar Hydrogen Evolution from Neutral Water, *Joule* 2 (2018) 537–548, <https://doi.org/10.1016/j.joule.2018.01.012>, <https://doi.org/>.
- [16] M. Grossberg, J. Krustok, J. Raudoja, K. Timmo, M. Altsaar, T. Raadik, Photoluminescence and Raman study of Cu $_2$ ZnSn(Se xS $_1 - X$ ) $_4$  monograins for photovoltaic applications, *Thin Solid Films* 519 (2011) 7403–7406, <https://doi.org/10.1016/j.tsf.2010.12.099>, <https://doi.org/>.
- [17] S. Huang, W. Luo, Z. Zou, Band positions and photoelectrochemical properties of Cu $_2$ ZnSnS $_4$  thin films by the ultrasonic spray pyrolysis method, *J. Phys. D. Appl. Phys.* 46 (2013), <https://doi.org/10.1088/0022-3727/46/23/235108> <https://doi.org/>.
- [18] A. Hankin, F.E. Bedoya-Lora, J.C. Alexander, A. Regoutz, G.H. Kelsall, Flat band potential determination: avoiding the pitfalls, *J. Mater. Chem. A.* 7 (2019) 26162–26176, <https://doi.org/10.1039/c9ta09569a>, <https://doi.org/>.
- [19] M. Metikoš-Huković, Z. Grubač, S. Omanovic, Change of n-type to p-type conductivity of the semiconductor passive film on N-steel: enhancement of the

pitting corrosion resistance, J. Serbian Chem. Soc. 78 (2013) 2053–2067, <https://doi.org/10.2298/JSC131121144M>, <https://doi.org/>.